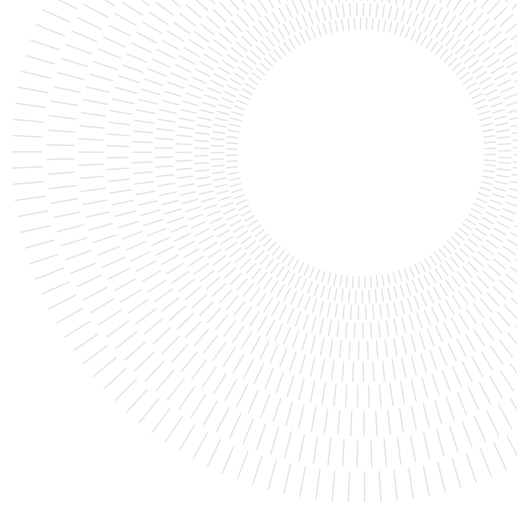




POLITECNICO
MILANO 1863

**SCUOLA DI INGEGNERIA INDUSTRIALE
E DELL'INFORMAZIONE**



Transient simulation of the DRS deactivation

FINAL REPORT FOR THE PROJECT OF THE COMPUTATIONAL FLUID DYNAMICS COURSE

Group number : 19

Thomas Magni, 10672007

Pietro Ravanelli, 10663836

Andrea Sacco, 10938373

Marco Schifone, 10683447

Lecturers:

Dr. Barbara Re

Dr. Tommaso Bellosta

Tutor:

Dr. Tommaso Bellosta

1. Problem statement

This work presents a computational fluid dynamics analysis of the DRS (Drag Reduction System) of an high performance car. Our intention is to investigate the aerodynamic behaviour of a 2D two-element rear wing under the 2023 *Formula 1* regulations, determining the effects of the flap rotation with particular focus on the transient behaviour of the aerodynamic coefficients.

1.1. Background

The rear wing of an *F1* car is responsible for the 20% of the overall downforce, thus its design it is crucial in order to reach high level of vertical load. The downforce can increase the maximum lateral and longitudinal forces on the tyres, resulting in an increase in cornering speed and better performance in braking and acceleration. However, in the straights the car needs to have as less drag as possible in order to reach the maximum speed. Improving one of the aspects above will always influence the other, hence they need to be carefully balanced. The DRS is an overtaking aid that works with an actuator which allows the rotation of the flap of the rear wing during the straights when a pilot is less than one second apart from the driver in front. Introduced in *Formula 1* in 2011, the DRS allows a reduction in the overall drag of the car of approximately 15% but also with a consequent loss of downforce, the result is an increase in the top speed of approximately 20 kph, which enhances the possibility of overtaking.



Figure 1: DRS in open and closed configurations.

1.2. Introduction to the problem

From this brief paragraph about what is the Drag Reduction System and how it works, it is clear that while the opening phase occurs at the beginning of a straight line, its closure occurs towards the conclusion and usually just before a corner: the deactivation phase is for sure more interesting and complicated since it has the objective to ensure that the car returns to the maximum levels of downforce when it is approaching the braking and cornering zone, in order to ensure the optima performances. After the analysis of the change in the aerodynamic loads of the wing between the open and closed configurations, the focus of this study will be on the transient movement of the flap, in order to verify the behaviour of the aerodynamic coefficients during the deactivation of the DRS.

1.3. Hypothesis

Within the framework of a CFD course project, the problem that we are going to analyse involves a series of simplifications compared to the real-world scenario. Nevertheless, proper modelling choices can yields results at a sufficient level of accuracy for our goals.

Since the available computational resources were limited, the flow over the rear wing was studied as a *2D* problem. Due to this hypothesis, the *3D* aerodynamic effects, such as the presence of tip vortices will not be accounted for. However, in the context of an *F1* rear wing the presence of the endplates will limit *3D* effects and the results obtained can be considered a good approximation. Another difference is that we are considering a free air stream investing our profiles, neglecting the interaction between the body of the car and the rear wing. Related to this, it is noteworthy to say that the opening phase will always take place behind another car, in its wake, where conditions are for sure not steady. It is also important to mention the fact that we are dealing with a mathematical model that is by definition an abstraction of physical reality.

1.4. Geometry definition

The first step of this study is the selection of the airfoils for the rear wing, which is based on the constraints that are imposed by the 2023 *Formula 1* technical regulations [1]. The rear wing must contain only two sections and it must lie inside a regulation volume. As this study is focused only on the multi-element wing, the control volume that needs to be taken into account is *RV-RW-PROFILES*, which will set requirements on the dimensions of the airfoils. The chord length is chosen to be 200 mm for the first airfoil, known also as main airfoil, and 100 mm for the rearmost airfoil, known also as flap airfoil. Moreover, the vertical gap between the two profiles must be between 10 mm and 15 mm in the closed configuration. In order to fulfil the technical requirements, but also to facilitate the creation of the sliding mesh, the vertical gap chosen is 12 mm, for similar reasons an overlap between the profiles has been avoided, and the horizontal distance is 0.75 mm. Then the shape of the aerofoil needs to be chosen, since the aim of this project is not aerodynamic optimisation of the rear wing, for simplicity's sake, the aerofoil chosen was the NACA 6412. It belongs to the NACA 4-digit series, which is a common parameterisation used in aerodynamics, since it involves only three parameters:

1. Maximum camber, expressed as a percentage of the chord.
2. Distance of the maximum camber from the leading edge of the airfoil, expressed in tenths of the chord.
3. Maximum thickness, expressed as a percentage of the chord.

In the closed configuration, the angles of attack of the main airfoil and the flap are $\alpha_{main} = 0^\circ$ and $\alpha_{flap,closed} = -30^\circ$ respectively. In order to simulate the opening movement of the DRS, a rotation of 30° of the flap is imposed with respect to its trailing edge. All the geometric parameters are shown in Table 1.

$c_{main} = 200 \text{ mm}$	$c_{flap} = 100 \text{ m}$	$\alpha_{main} = 0^\circ$	$\alpha_{flap,closed} = -30^\circ$	$h_v = 12 \text{ mm}$
-----------------------------	----------------------------	---------------------------	------------------------------------	-----------------------

Table 1: Geometric characteristics of the airfoils.

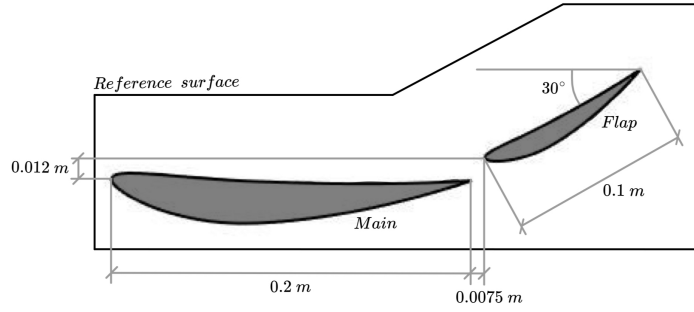


Figure 2: Geometry of the problem with profiles and reference surface.

2. Numerical simulation methodology

One of the ideas to achieve reliable results for our unsteady problem involving the movement of the flap is to initially analyse a steady situation for both the open and closed configurations. This preliminary phase will provide reference comparisons for the two limit positions of the DRS while executing the unsteady simulations.

2.1. Mesh construction

In our study we needed two type of mesh, one for the steady state cases (standard single-zone mesh) and a slightly different one for the unsteady problem, in which a multi-zone mesh is needed in order to perform the rotation of the flap around its trailing edge. To generate the mesh the software *gmsh* [2] has been employed. For both of them, a circular domain centred on the leading edge of the main profile has been chosen. The parameters used in the mesh definition are:

- R : radius of the circular domain (i.e. farfield distance from the leading edge of the main profile)
- H : dimension of the cells at farfield
- h : dimension of the cells near the airfoils

In addition, the elements near the airfoils are proportionally refined towards the leading edge and the trailing edge of both the profiles, where the curvature and the flow properties change faster.

2.1.1 Single-Zone Mesh

In the single-zone mesh, it was crucial the choice of the refinement in the most critical areas of the domain. All these refinements are imposed with *gmsh* fields *Distance* and *Threshold* by relating element sizes to h .

The first refinement has been placed around the two profiles, where the flow properties change in a significant way with respect to the outer domain. In particular it was created a box around the two profiles and a further refinement field around the second half of the flap, where a region of separated flow is expected (Figure 3). Another refinement is needed to capture the behaviour of the flow in the wake region. To do so we identified the wake location in the two configurations to add a further refinement in that area, which is progressively downsized until a distance of 10 chords as shown in Figure 4. By adopting this approach, it was possible to diminish the overall number of cells but also to enhance the precision of the results through the implementation of a more focused grid. Regarding the interaction between elements and profiles, it is important that the mesh near the wall is properly sized to ensure accurate simulation of the flow field. Thus an unstructured mesh has been used in all the domain, except for the boundary layers of the two airfoils, where a structured mesh is preferred (Figure 5).

The size of the cells at the wall has been set in order to get the desired value of $y^+ \sim 1$. The width of the elements is related to the parameter h and the height of the boundary layer was chosen to suitably capture its development over the two airfoils.

A mesh convergence study, which results are shown in section 3.1, facilitated the identification of the optimal values for R , H , h .

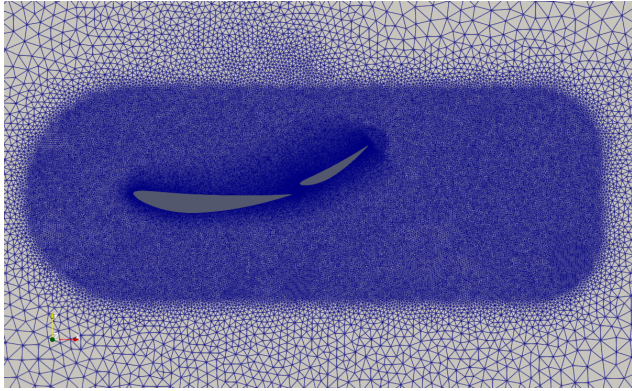


Figure 3: Refinement box on profiles.

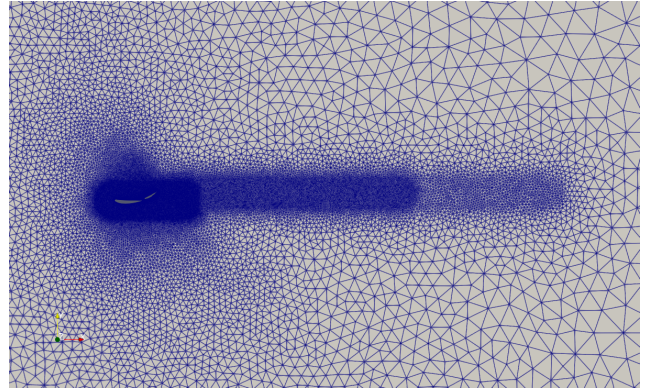


Figure 4: Refinement on the wake.

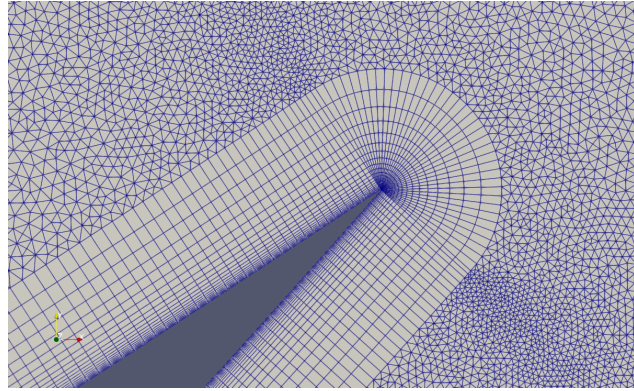


Figure 5: Boundary layer of the trailing edge of the flap.

2.1.2 Multi-Zone Mesh

The Multi-zone mesh derives from the single-zone design with specific modifications. To accommodate the rotation of the flap, we implemented two separate meshes: given the significant rotation angles involved, mesh deformation would have resulted in excessive distortions in the elements; therefore, we opted for a sliding mesh approach.

Then two zones were defined as follows: an inner zone where the flap has been placed, and the outer zone with the main profile. The inner zone is defined as a circular domain centred at the trailing edge of the flap, featuring a smaller radius compared to the farfield one: this zone accommodates both the flap and its boundary layer. The second mesh, or outer zone, has the same features of the single-zone one, but it incorporates a circular void corresponding to the location of the smaller circle of the first zone. Our multi-zone mesh closely resembles the single-zone counterpart, featuring the addition of the interface circle as main distinction.

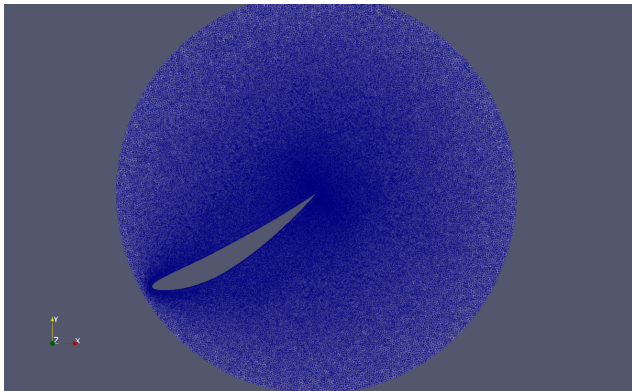


Figure 6: Inner zone mesh.

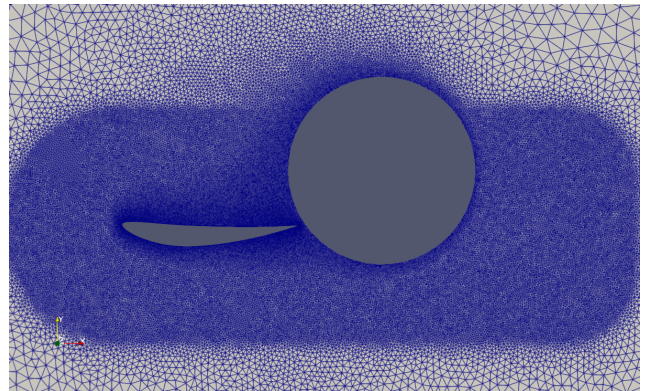


Figure 7: Outer zone mesh.

The primary challenge that has been encountered revolved around determining the refinement at the interface between

the two zones. We had two potential solutions: one involved making localised adjustments specifically on the interface between the trailing edge of the main profile and the leading edge of the flap to achieve finest refinement. The other solution entailed maintaining a constant h across all points along the circular interface. In the final mesh configuration, the decision was to maintain a constant value for h along the interface circle. This choice was made as it was recognised that employing varying refinements on the interface could potentially lead to complications when the circular structure starts rotating. The concern was that such an approach might result in excessively long elements in close proximity to the interface during the rotation, because the two meshes would have no more coincided.

Figures 9 and 8 highlight which is the zone where the transition from a single to a multi-zone mesh has a more pronounced impact.

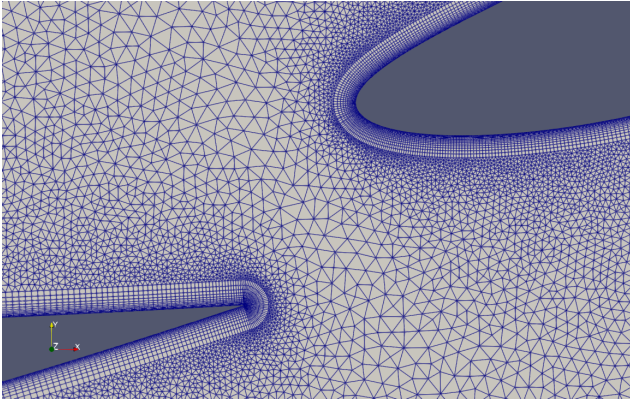


Figure 8: Zoom on the interface of the multi-zone.

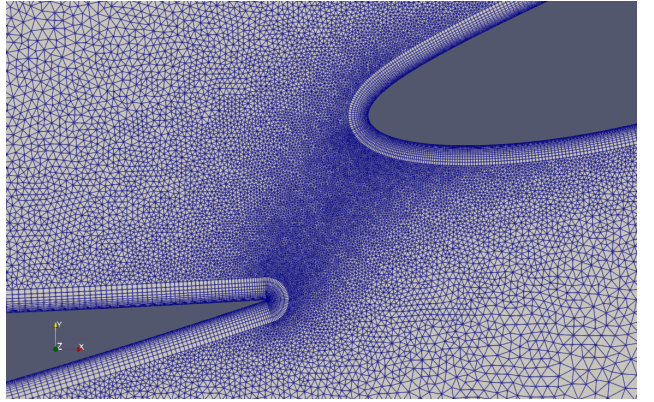


Figure 9: Zoom on the region between the two profiles.

2.2. Numerical methods

In the following section will be provided a description of the numerical schemes that were selected for this simulation, as well as the turbulence model and the boundary conditions. The software that has been used for this project is *SU2* [3], an open source computational analysis tool developed by Stanford University.

2.2.1 Solver and numerical scheme

For turbulent flows we have to solve the Reynolds-Averaged Navier-Stokes (RANS) equations: in doing this, advantages and disadvantages of the approach must be considered and a deep analysis of the results must be taken into account. In order to solve the closure problem a turbulence model is needed and this part is exploited in Section 2.2.2.

The numerical scheme adopted for this work is the second order Roe scheme with MUSCL approach (Monotonic Upstream-Centred Scheme for Conservation Laws). The classic Roe scheme is a first order method and is an approximate Riemann solver based around the Godunov scheme and works by looking for an estimate for the intercell numerical flux at the interface between two computational cells. The MUSCL approach extends the Roe scheme to a second or higher-order accuracy by using slope limiters and other techniques to incorporate gradient information within each cell, thus enhancing the overall accuracy of the simulation. Moreover, FGMRES is chosen as the linear solver and the ILU method is used as preconditioner.

2.2.2 Turbulence model: $k - \omega$ SST

The turbulence model chosen is the $k - \omega$ SST, a two equations model, which means that in addition to the conservative equations it solves two transport equations for the turbulent kinetic energy k and the turbulent dissipation rate ω . The Shear Stress Transport (SST) formulation was developed by Menter (1994) [4] in order to improve the prediction of flows under adverse pressure gradient. The key innovation of the SST model is its blending technique, which merges the $k - \omega$ model in the near-wall region with the $k - \epsilon$ model for the remainder of the flowfield. In order to achieve this result the blending function F_1 has been introduced, which is an hyperbolic function that is used for a smooth transition between

the two models. The two transport equations are:

$$\frac{\partial k}{\partial t} + U_i \frac{\partial k}{\partial x_i} = \frac{\partial}{\partial x_j} \left(\nu \frac{\partial k}{\partial x_j} + \frac{\nu_t}{\sigma_k} \frac{\partial k}{\partial x_j} \right) + P_k - C_\mu \omega k \quad (1)$$

$$\frac{\partial \omega}{\partial t} + U_i \frac{\partial \omega}{\partial x_i} = \frac{\partial}{\partial x_j} \left(\nu \frac{\partial \omega}{\partial x_j} + \frac{\nu_t}{\sigma_\omega} \frac{\partial \omega}{\partial x_j} \right) + \gamma \frac{k}{\nu_t} P_k - \beta \omega^2 + (1 - F_1) 2\sigma_\omega \frac{1}{\omega} \frac{\partial k}{\partial x_i} \frac{\partial \omega}{\partial x_i} \quad (2)$$

And the blending function F_1 is defined as follows:

$$F_1 = \tanh(\arg_1^4) \quad (3)$$

$$\arg_1 = \min \left(\max \left(\frac{k^{0.5}}{C_\mu \omega y}, \frac{500\nu}{y^2 \omega} \right), \frac{4\rho \sigma_\omega k}{C_{Dk\omega} y^2} \right) \quad (4)$$

Away from the wall the blending function is zero (leading to the $k - \epsilon$ model), while F_1 is equal to 1 close to the surface and the Equation 2 becomes the original ω equation proposed by Wilcox [5]. The turbulent eddy viscosity for the $k - \omega$ SST model is defined as:

$$\nu_t = \frac{a_1 k}{\max(a_1 \omega, SF_2)} \quad (5)$$

where F_2 is another blending function and S is the magnitude of the shear strain. Thus when SF_2 is greater than $a_1 \omega$ the eddy viscosity is limited, which implies a better agreement with experimental results of separated flows. For the above reasons the SST model proposed by Menter is recommended for aerodynamic application since it is the only two equations model that has shown the ability to accurately predict pressure-induced separation.

2.2.3 Boundary and freestream conditions

In order to guarantee a good representation of the problem, it is crucial to set the right boundary conditions at all interfaces. At the farfield the freestream conditions like temperature, pressure, Mach number, turbulence intensity and the eddy viscosity ratio are imposed. The values of all the flow conditions are shown in Table 2.

Flow condition	Value
Temperature	288.15 K
Pressure	101325 Pa
Dynamic viscosity	$1.7895 \times 10^{-5} \text{ m}^2/\text{s}$
Mach number	0.15 [-]
Turbulence intensity	0.3 %
Eddy viscosity ratio	2 [-]

Table 2: Flow conditions.

The interface serves as a non-physical surface separating the inner and the outer meshes, which is why there are no specific boundary conditions to impose on it. When it comes to the profiles, a non-slip condition needs to be enforced, designating them as solid bodies. Additionally, markers have been assigned to these profiles to make the solver monitor and compute significant quantities like lift and drag coefficients. Another relevant parameter to mention is the CFL, which is set as adaptive, in order to speed up the simulation and avoid possible numerical instabilities. Finally, the convergence variable chosen was the root mean square of the density residual, which was set as 10^{-8} for both the two zones.

2.3. Sliding mesh with Python wrapper

In order to represent the real deactivation of the DRS the flap has to start rotating from 0° and then to stop at -30° in 0.1 s, while the simulation has to continue after the flap stops rotating, in order to study how the wake changes and the flow stabilises. It was not possible to study this type of problem with the *SU2* software alone because with a multi-zone simulation the rotation rate is defined at the beginning and can not be changed anymore, so the flap would keep rotating for the whole simulation. Consequently *Python wrapper* has been employed to control the simulation and change the rotation rate of the flap in every time step. This is why a Python file was created and thanks to it we were able to define the number of iterations before, during and after the rotation, when it finally reached the final position.

It was also created a specific function that defines the angle of the profile and so the rotation rate. This function was constructed by means of the sine function and varying it in magnitude and argument to fit the problem. The sine function was chosen because it was one of the smoothest way to reach that angle in the given short time. As a result for every time step the function defines an angle θ as shown in Figure 10. After that a rotation rate was calculated based on the Δt and the configuration file was uploaded with the new rotation rate.

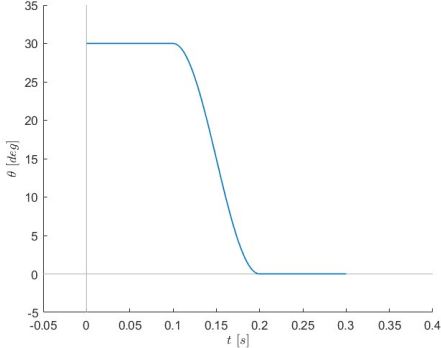


Figure 10: Function for the rotation angle of the flap.

One of the most difficult problems that we had to deal with was to write the code in Python and understand how our Python file was reading and modifying the configuration files that govern our simulation. At the end the best solution to control the rotation rate at each time step was to use the restart-flow file provided by the *SU2* solver and for every time step to restart our solution from the previous one. As the first simulation was launched it was evident that it was necessary to use a restart-flow file of a steady simulation for the first time step to reduce the computational cost. To ensure that our flow closely resembled the conditions observed in the steady simulation, we began the rotation of the flap after a certain number of time iterations, typically around 5. This deliberate delay was implemented to allow the flow to stabilise before further analysis, providing a more accurate representation of the desired conditions.

3. Results

3.1. Mesh independence study

As detailed in Section 2.1.1, our mesh relies on multiple parameters. When dealing with a CFD simulation it is important to ensure that the results are grid independent, which means that they do not change with the grid size and with the number of elements of the mesh. The mesh independence study can be performed by varying one by one its parameters while keeping the others constant. Since our problem treats two different configurations, we decided to perform the analysis on the most challenging one from the aerodynamic point of view, namely the closed one, due to the region of separated flow expected. The parameters that will be investigated during this study are R , H , h .

Firstly, our focus was on investigating the farfield parameter R . We selected values for R as multiples of 20, 50, 100, and 200 times the chord length of the main profile. For each of these configurations, we examined both the total lift coefficient C_L and the total drag coefficient C_D to determine the point at which our problem ceased to depend on this parameter. As illustrated in Figure 11 and 12, satisfactory results were already achieved when the parameter R was set to 100 times the chord length, so that value was chosen.

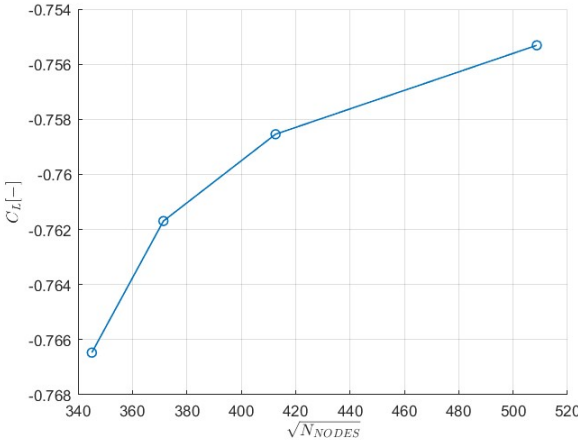


Figure 11: C_L obtained by varying the R .

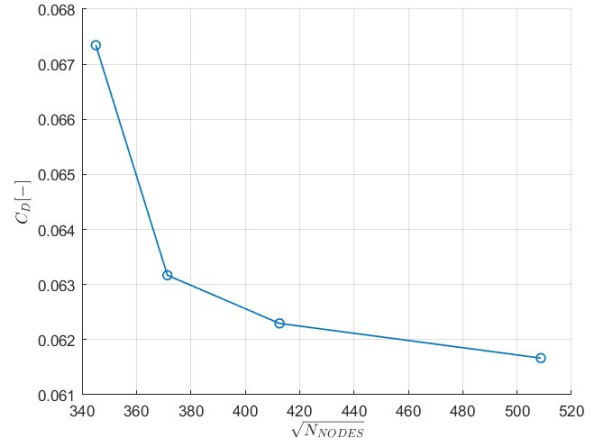


Figure 12: C_D obtained by varying the R .

Subsequently, we delved into an analysis of the other farfield parameter, H . The values of H (all expressed in meters) that were tested are 2, 1.2, 1, 0.8, 0.6. However, the results yielded less significance, leading us to conclude that our problem lacked a substantial dependence on this particular parameter.

Lastly, we analysed the parameter h . Given its impact on both the boundary layer and the wake field characteristics, multiple simulations were conducted to conclusively confirm the independence of our problem from variations in h . Specifically, values of h (all expressed in meters) equal to 0.0035, 0.004, 0.0045, 0.005, 0.006, 0.008, and 0.012 were selected for analysis. The outcomes for C_L and C_D can be observed in Figure 13 and 14. A particular behaviour was observed while performing mesh convergence: decreasing too much the value of h had as an outcome a slight worsening of the results. This is due to the generation of elongated elements in the boundary layer region. Also for this reason h equal to 0.005 was chosen.

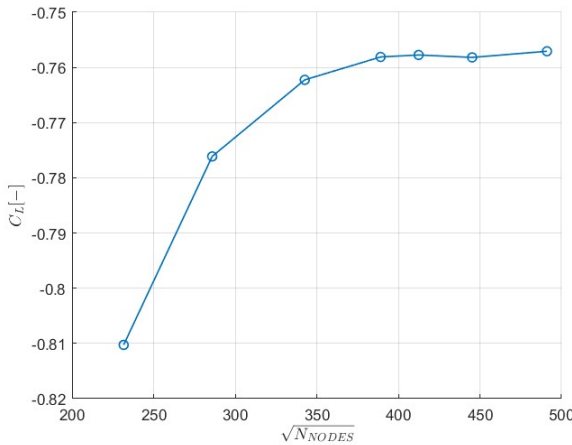


Figure 13: C_L obtained by varying the h .

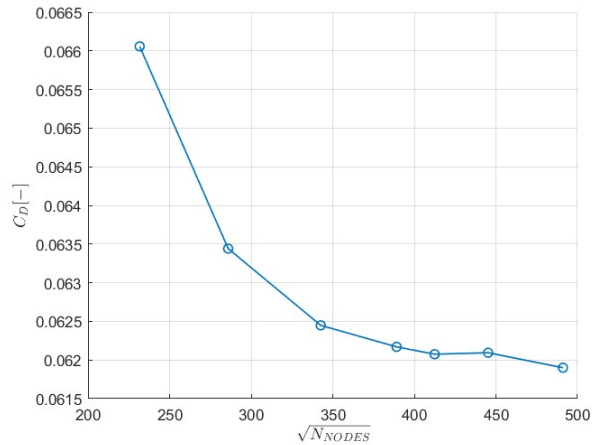


Figure 14: C_D obtained by varying the h .

Ultimately, we decided to adopt the parameters outlined in Table 3.

Grid parameter	Value
R	20 m
H	0.8 m
h	0.005 m

Table 3: Selected grid parameters.

Our choice was informed by a thorough examination of the percentage error, computed with our choice as the reference value, as illustrated in the Figures 15 and 16. For both the parameters studied the error is small: less than 1% for h in the finest meshes and less than 2% for R .

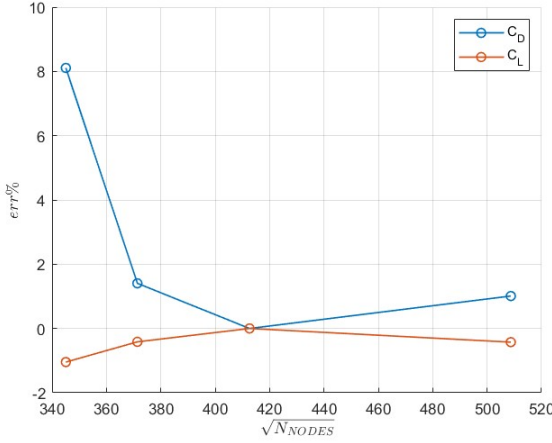


Figure 15: Percentage error obtained by varying R .

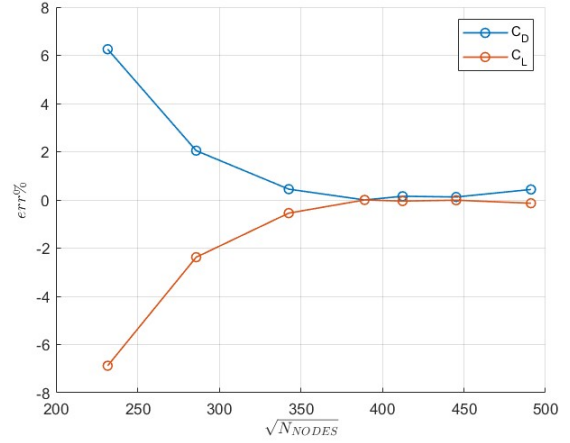


Figure 16: Percentage error obtained by varying h .

3.2. Multi-zone mesh validation

Due to the high computational cost of multi-zone mesh simulations, we decided not to repeat the validation, but to compare the results of single-zone simulations with the ones of the multi-zone. This was certainly less accurate but, apart from the interface zone, the mesh we adopted is approximately the same. The comparison was done for both closed and open configurations. The results we came at are shown in Table 4. The aerodynamic coefficients are similar and the errors are clearly due to the introduction of the interface.

Closed configuration	Single-zone Multi-zone Percentage error	$C_L \text{ tot} = -0.758106$ $C_L \text{ tot} = -0.737455$ $\text{err}_{CL} = 2.72\%$	$C_D \text{ tot} = 0.06217$ $C_D \text{ tot} = 0.061452$ $\text{err}_{CD} = 1.15\%$
Open configuration	Single-zone Multi-zone Percentage error	$C_L \text{ tot} = -0.214766$ $C_L \text{ tot} = -0.213786$ $\text{err}_{CL} = 0.46\%$	$C_D \text{ tot} = 0.007708$ $C_D \text{ tot} = 0.007727$ $\text{err}_{CD} = 0.25\%$

Table 4: Multi-zone vs single-zone meshes.

A further analysis was also conducted on the multi-zone mesh featuring varying levels of refinement along the interface to increase the element density in the region of interest. We compared this unsteady simulation with a similar one employing a constant number of elements on the interface circle. The results showed a small percentage error during the rotation (less than 2% for C_D and less than 0.3% for C_L at every time step). However, convergence issues arose in the last part of the simulation when the two meshes no longer coincided. Consequently, we opted for a mesh with a constant number of elements on the interface circle.

3.3. Time step sensitivity analysis

For the unsteady simulation, also the time step parameters needed to be tuned in order to have an accurate time marching. The two parameters we considered in this analysis are the following:

- N_{ROT} : number of time iterations during the transient phase. Since the closing time of the DRS is a fixed parameter, N_{ROT} defines the time step of the simulation, which is the same for both the closing part and the post-closing one.
- N_{AFT} : number of iterations in the post-transient phase. This parameter sets the end time of the simulation which must be long enough to allow the flow stabilisation. Since the time step is fixed, it was more intuitive to investigate the ratio N_{AFT}/N_{ROT} .

At first we proceeded by choosing a series of values for N_{AFT}/N_{ROT} and computing the error of C_D and C_L with respect to the steady simulation. The ratios investigated are 1, 2, 3.5, 5, 7 and the chosen value is 5, which yields to errors on C_D and C_L under 0.5% as shown in Figure 17.

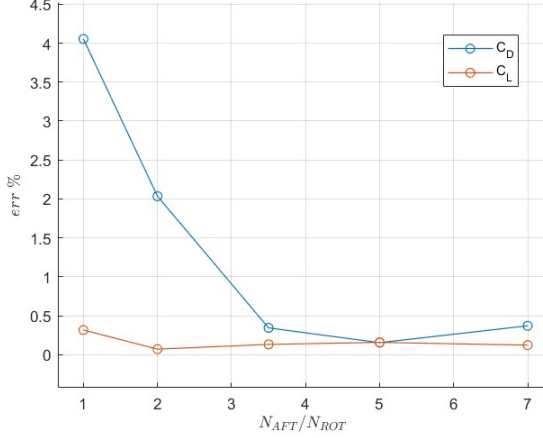


Figure 17: Percentage error varying N_{AFT}/N_{ROT} .

The second parameter under consideration was the number of time iterations during the rotation, denoted as N_{ROT} . In the initial simulation, we opted for $N_{ROT} = 50$; however, we encountered challenges as each time iteration demanded over 4000 outer iterations. This resulted in an excessively long total computational time. We hypothesised that this issue stemmed from a combination of a prolonged time step, denoted as Δt , and a high rotation rate, causing difficulties for the solver to converge effectively. After that, we managed to run some simulation with different N_{ROT} and so time steps. In particular we chose N_{ROT} equal to 100, 150, 200, 300. Through these simulations, we achieved satisfactory results within a reasonable computational time. It became evident early on that the values of our lift coefficient C_L and drag coefficient C_D were not significantly influenced by variations in Δt . However, as elaborated in Section 3.5, employing a finest time step allowed us to observe and analyse specific phenomena. In Figures 18 and 19 the percentage error is provided at the common time steps calculated with the previous simulation as reference value.

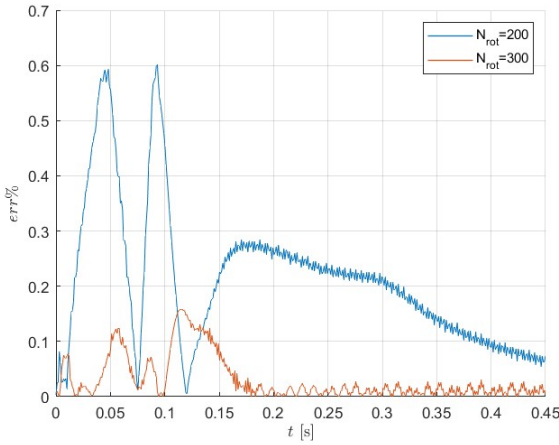


Figure 18: Percentage error in every common time step for C_L .

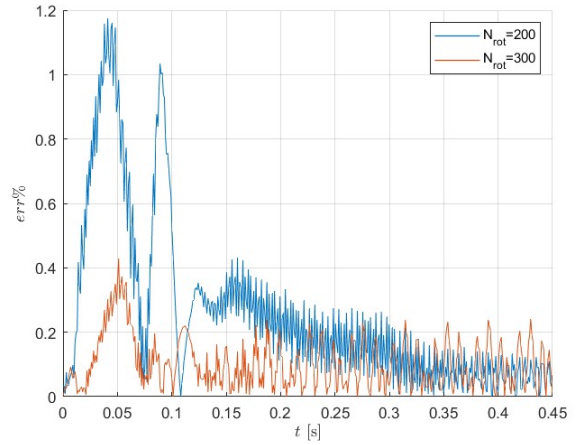


Figure 19: Percentage error in every common time step for C_D .

As demonstrated, the percentage error is remarkably small, particularly in the case of C_L . Specifically, when comparing the 300-iteration simulation to the 200-iteration one, the error is less than 0.5% for both the considered aerodynamic coefficients.

3.4. Steady state simulation results

After conducting an exhaustive analysis on the mesh and finalising the parameters, the ultimate simulation was executed for both configurations with the DRS open and closed. The obtained results are detailed in Table 5 and Figures 20, 21, 22 and 23. A clear advantage in terms of drag reduction is evident when running with the DRS in the open configuration. The reduction in total drag is 87.4%, while the overall lift shows a decrease of 71% which are aligned with the order of magnitude of the expected decrease in freestream conditions from previous studies [6].

DRS-Open	$C_{L\ tot} = -0.213786$	$C_{L\ main} = -0.166040$	$C_{L\ flap} = -0.047746$
	$C_{D\ tot} = 0.007727$	$C_{D\ main} = 0.000538$	$C_{D\ flap} = 0.007189$
DRS-Closed	$C_{L\ tot} = -0.737455$	$C_{L\ main} = -0.447358$	$C_{L\ flap} = -0.290097$
	$C_{D\ tot} = 0.061452$	$C_{D\ main} = -0.035740$	$C_{D\ flap} = 0.097192$

Table 5: Results of the steady state simulation.

Figures 20, 21 show the velocity field around the rear wing for the closed and open configurations respectively. It can be clearly seen that due to the null angle of attack of the profiles, and with the chosen airfoil shape, which is not optimised for motorsport applications, thus with a lower camber compared to the *Benzing* airfoils [7] family, the level of downforce generated in this condition is very low compared to the baseline closed configuration, making this configuration not suitable for cornering and braking conditions. For the same reasons, it can be observed from the closed configuration (Figure 20), since the angle of attack of the main airfoil is null, the major source of drag comes from the separation of the flow over the flap due to the high angle of attack. A first possible solution to this problem is the use of a *Gurney flap* a small device placed on the rearmost airfoil perpendicular to its pressure side, which allows to increase the maximum value of the lift coefficient with possible positive effects on the drag coefficient as well. Moreover, introducing an overlap between the two airfoils, changing the angle of attack of the main profile and reducing the vertical gap to the minimum value allowed, could be a beneficial choice as well.

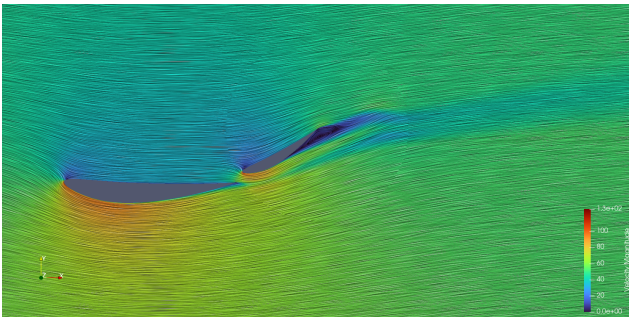


Figure 20: Velocity field with DRS deactivated.

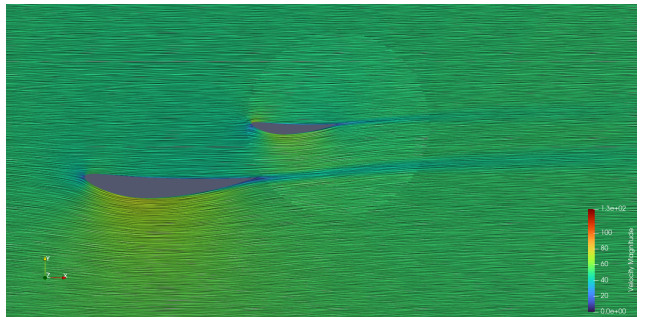


Figure 21: Velocity field with DRS activated.

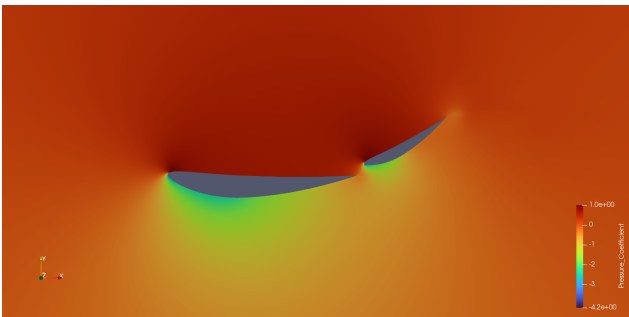


Figure 22: Pressure coefficient field with DRS deactivated.

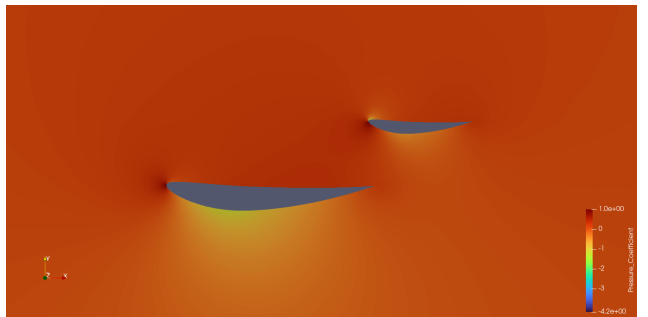


Figure 23: Pressure coefficient field with DRS activated.

As depicted, the configuration with the DRS open (flap at 0° AoA) exhibited no issues and the obtained results aligned with expectations, while we met a problem with all the simulations that we run with the DRS closed. The identification of a negative value for $C_{D\ main}$ is atypical, but this trend persisted across all simulations conducted during our exploration of mesh independence. Unfortunately, we encountered difficulty in finding comparable issues in existing literature to validate our results. Particularly challenging was the absence of specific values for the individual profile's C_D and C_L in the available reports, as most literature only provided the total coefficients. However, from a recent study [8] it is possible to find that for a particular configuration, especially in terms of angle of attack of the main profile, vertical and horizontal gap between the two profiles, a negative contribute by some sections of an inverted multi-element wing can be seen. As outlined in Table 6, the negative contribution to the C_D coefficient arises from the pressure component.

This observation is further elucidated in Figure 24, where the pressure distribution reveals consistent values on the entire pressure side. However, on the suction side, particularly on the right segment, the C_p exhibits a higher value compared to the left side, explaining the resultant force directed towards the left.

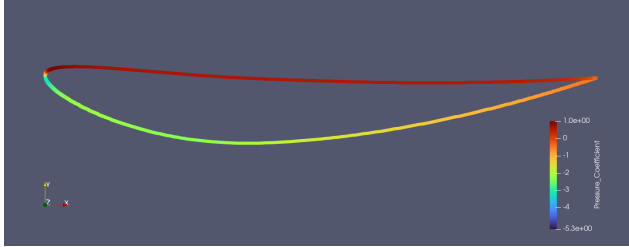


Figure 24: C_p on surface of the main airfoil.

$C_D \text{ main} = -0.035740$
$C_D \text{ pressure} = -0.037857 \text{ (105%)}$
$C_D \text{ friction} = 0.002117 \text{ (-5%)}$

Table 6: C_D contribution of the main airfoil.

Upon examining the flow field resultant during the post-processing in the closed configuration we identified the presence of a small laminar recirculation bubble close to the leading edge of the flap, as highlighted in Figure 25. The zone where it happened was where the boundary layer would separate due to the significantly high angle of attack. It is within this context that we understood the significance of the relative positioning of the two profiles: the main profile played a crucial role in reattaching the flow to the surface of the flap, inducing a transition from laminar to turbulent of the flap boundary layer (resulting in a delayed separation of the boundary layer). This outcome aligned with our goal for an efficient car's rear wing, where achieving a high lift coefficient with the minimum possible drag coefficient is essential. The laminar to turbulent transition can be seen in the plot of the turbulent kinetic energy in Figure 26, where it is possible to see a clear peak in it that is probably due to the transition and a consequent peak in its production term, then once the turbulent flow is fully established the flow may stabilise, leading to a reduction in the turbulent kinetic energy.

As part of the post-processing, the tangential skin friction coefficient C_f was computed and its behaviour on the suction side is shown in Figure 27, where it is plotted along the chord. The tangential skin friction coefficient accounts for the part of the friction that is aligned with the tangent of the airfoil at each point. A positive value of the C_f indicates that the flow is attached to the surface, on the opposite a negative values suggest a flow separation, where the flow is moving in the opposite direction to the airfoil surface. The graph shows a positive peak near the leading due to the presence of a stagnation point, which can increase substantially the skin friction, than it is possible to appreciate the small laminar recirculation bubble very close to the position of the leading edge. As it was explained previously the flow then reattaches and the tangential skin friction returns positive. Corresponding to the large separation of the flow on the back part of the flap (Figure 20) the C_f becomes negative again.

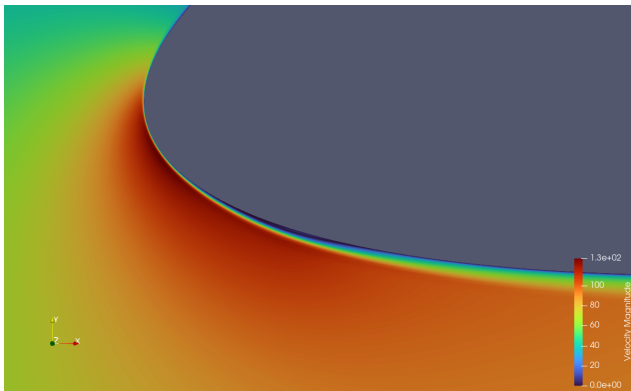


Figure 25: Recirculation bubble in the velocity field.

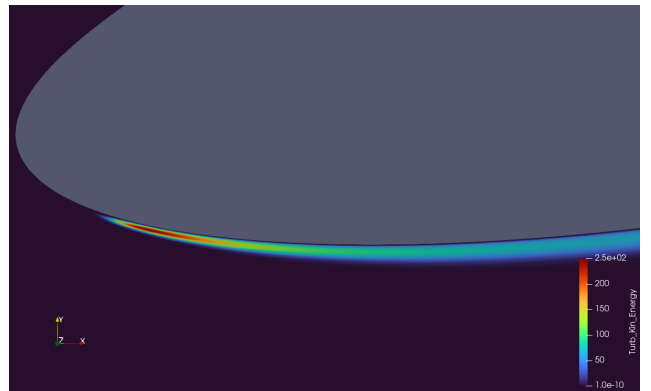


Figure 26: Turbulent kinetic energy.

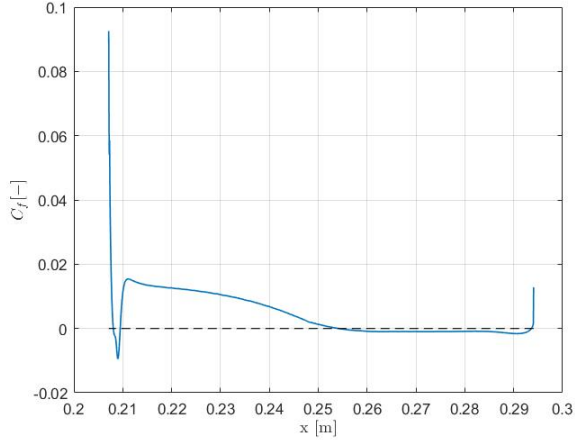


Figure 27: Tangential skin friction coefficient on the suction side of the flap along the chord.

3.5. Unsteady simulation results

With a robust base of results and steady simulations, we were now allowed to use them as restarting points for a series of unsteady ones. The real effects of the flow field over the profiles during the transient of the DRS could be appreciated by plotting C_L and C_D over time and comparing them with what could be seen with *ParaView*.

A first look at the two graphs obtained below (Figure 28 and Figure 29) reflects what one would expect from the operation of a movable wing mounted on a racing car: namely, C_L and C_D are progressively increasing (with C_L moving towards negative values as it becomes a downforce configuration) during closure, until they stabilise at values obtained from steady-state simulations after a brief adaptation to the new configuration. While the lift coefficient quickly stabilises, the drag coefficient requires more time to converge; we attribute this delay primarily to the unsteadiness of the wake, which significantly influences the C_D .

The most significant phase from a physical standpoint during the transient is undoubtedly the final phase ($0.09s \div 0.11s$), where the peaks in both parameters highlight the impulsive nature of the movement which occurs at a higher speed compared to the characteristic times of the flow settling.

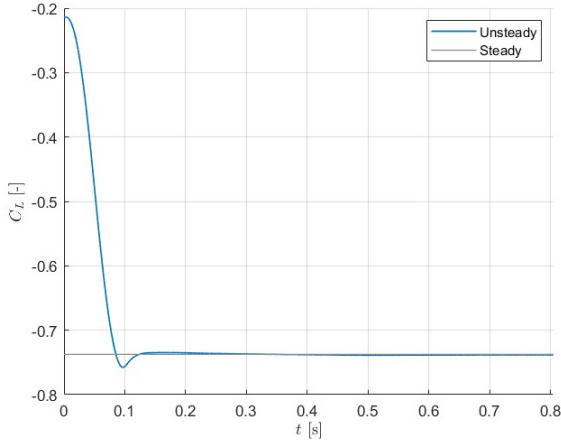


Figure 28: C_L behaviour during DRS deactivation.

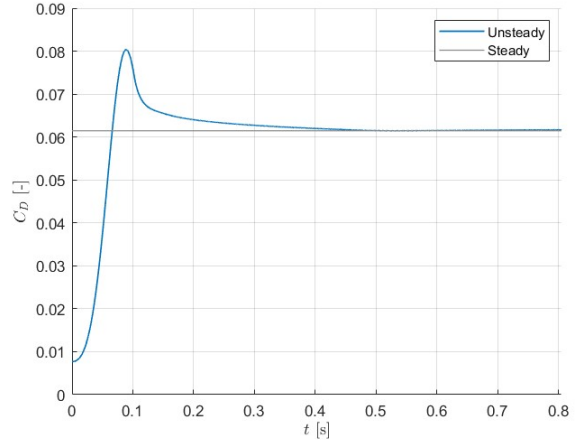


Figure 29: C_D behaviour during DRS deactivation.

A notable behaviour of the parameter C_D is shown in Figure 30 where oscillations caused by flow separation become evident; a more in-depth analysis of the phenomenon is conducted by examining the trend of the curve once the DRS has been closed (Figure 31).

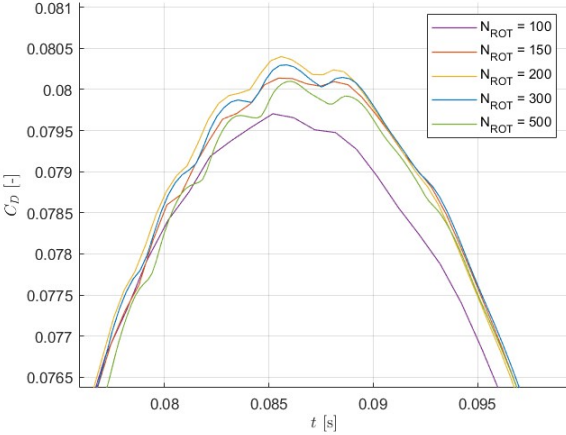


Figure 30: Zoom on oscillations at $\theta \sim 28^\circ$.

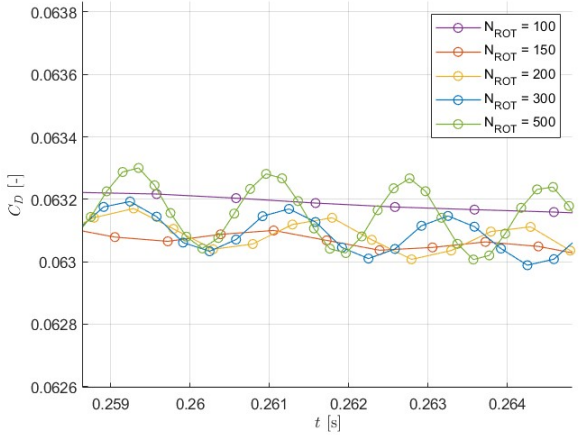


Figure 31: Zoom on C_D oscillations in closed configuration .

In Figure 32 it is displayed the separation zone with two vortices at the trailing edge of the flap, highlighting the vortex shedding phenomenon. The frequency of the vortex shedding is characterised by the flow velocity and the shape of the body. From the oscillation of the C_D plotted in Figure 31, it can be seen that there is not a unique frequency and amplitude, instead they vary with N_{ROT} . This could be due to the aliasing on the sampling frequency which is not high enough to catch the actual frequency of the phenomenon. By analysing the data presented in Figure 31, we have the opportunity to calculate the empirical frequency ($\sim 580\text{Hz}$) of the phenomenon through our highly refined simulation. However, it is evident that the current data set consists of only 10 points for every period. To enhance the characterisation of the phenomenon, it is essential to have a minimum of 30 points for each period. Achieving this desired level of granularity would necessitate employing an exceedingly large value for the parameter N_{rot} (~ 1800) to comprehensively characterise the phenomenon. Unfortunately, this was out of our computational capability. In addition, knowing the exact vortex shedding frequency would be interesting from a structural point of view, so as not to couple with the structural natural frequencies and lead to resonance problems on the rear wing.

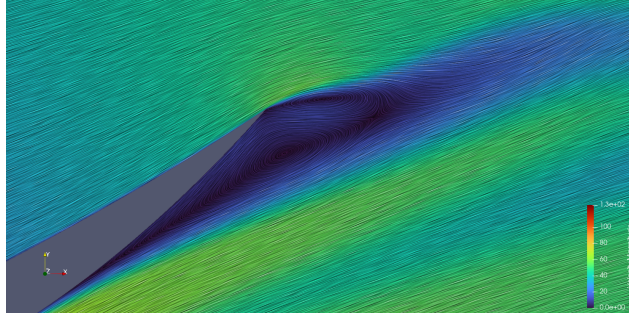


Figure 32: Recirculation bubble in the wake.

4. Conclusions

The purpose of our study was to investigate the aerodynamic behaviour of a Drag Reduction System under the Formula 1 regulations with a 2D model. We successfully obtained favourable results in our steady and unsteady simulation, as demonstrated in Section 3.4 and 3.5. These results allowed us to observe several characteristic phenomena of the system, including vortex shedding, a substantial separation zone at the trailing edge of the flap with its accompanying wake and the formation of a recirculation bubble just below the leading edge. It is crucial to recognise that all the results obtained are outcomes of various approximations. Therefore, they may not accurately represent the intricate reality of a Drag Reduction System. Nonetheless, our simulation serves as a valuable starting point to understand the workings of this system, given that such problems are not commonly addressed in the existing literature.

From Figures 28 and 29, it is evident that both C_L and C_D attain their peak values at $\sim 28^\circ$. Since this value is reached before the complete closure of DRS, this seems to suggest that we would obtain more aero performances stopping the rotation with a few moments in advance; actually it is a conclusion that would need a significant part of problem

optimisation, exploring configurations within the bounds of *F1* regulations to be confirmed or rejected. In *Formula 1* races, the Drag Reduction System (DRS) is automatically closed just before a turn when the driver starts braking. The goal is to maximise both coefficients at this critical moment, ensuring optimal adherence to the ground and maximum braking power. Certainly, exploring different angles of attack within the bounds of *F1* regulations could be an insightful analysis. Comparing the effects of various configurations on the aerodynamic coefficients would provide valuable insights into optimising the performance of the rear wing of the car: by systematically examining how variations of the angle of attack of the flap influence downforce, drag, and other aerodynamic characteristics, it is possible to enhance the overall efficiency and effectiveness of the DRS in the context of *Formula 1* racing.

As previously mentioned (Section 3.5), the convergence of C_L and C_D occurs at different moments. Since what is crucial for entering a turn with grip and stability is primarily the lift coefficient, we are pleased to observe that this condition is promptly established.

References

- [1] Fédération Internationale de l'Automobile. *2023 Formula 1 Technical Regulations*.
- [2] Gmsh. <https://gmsh.info/>.
- [3] SU2. <https://su2code.github.io/>.
- [4] F. Menter. Two-equation eddy-viscosity turbulence models for engineering applications. *AIAA Journal*, 32:1568–1605, 1994.
- [5] D. C. Wilcox. Reassessment of the scale-determining equation for advanced turbulence models. *AIAA Journal*, 26: 1299–1310, 1988.
- [6] M. Mendes R. Loucao, G. O. Duarte. Aerodynamic study of a drag reduction system and its actuation system for a formula student competition car. *Fluids*, 2022.
- [7] E. Benzing. Profili Benzing. <http://www.benzing.it/enrico.profili.htm>.
- [8] J. Ortega-Casanova F.J. Granados-Ortiz, P. Morales-Higueras. 3D CFD simulation of the interaction between front wheels and brake ducts and optimised five-element f1 race car front wings under regulations. *Alexandria Engineering Journal*, 2023.